Precision Determination of the Neutral Weak Form Factor of ⁴⁸Ca

(The CREX Collaboration)

```
D. Adhikari, H. Albataineh, D. Androic, K.A. Aniol, D.S. Armstrong, T. Averett, C. Ayerbe Gayoso, 5
    S.K. Barcus, V. Bellini, R.S. Beminiwattha, J.F. Benesch, H. Bhatt, D. Bhatta Pathak, D. Bhetuwal,
    B. Blaikie, <sup>10</sup> J. Boyd, <sup>11</sup> Q. Campagna, <sup>5</sup> A. Camsonne, <sup>6</sup> G.D. Cates, <sup>11</sup> Y. Chen, <sup>8</sup> C. Clarke, <sup>12</sup> J.C. Cornejo, <sup>13</sup>
    S. Covrig Dusa, M. M. Dalton, P. Datta, A. Deshpande, D. Dutta, D. Dutta, C. Feldman, E. Fuchev, 14
C. Gal, <sup>15,9,11,12</sup> D. Gaskell, <sup>6</sup> T. Gautam, <sup>18</sup> M. Gericke, <sup>10</sup> C. Ghosh, <sup>19,12</sup> I. Halilovic, <sup>10</sup> J.-O. Hansen, <sup>6</sup> O. Hassan, <sup>10</sup>
          F. Hauenstein, W. Henry, C.J. Horowitz, C. Jantzi, S. Jian, S. Johnston, D.C. Jones, O.C. Jones, 20, 6
         S. Kakkar, <sup>10</sup> S. Katugampola, <sup>11</sup> C. Keppel, <sup>6</sup> P.M. King, <sup>22</sup> D.E. King, <sup>23, 20</sup> K.S. Kumar, <sup>19</sup> T. Kutz, <sup>12</sup>
   N. Lashley-Colthirst, <sup>18</sup> G. Leverick, <sup>10</sup> H. Liu, <sup>19</sup> N. Liyanage, <sup>11</sup> J. Mammei, <sup>10</sup> R. Mammei, <sup>24</sup> M. McCaughan, <sup>6</sup>
   D. McNulty, D. Meekins, C. Metts, R. Michaels, M. Mihovilovic, 25, 26 M.M. Mondal, 12, 15 J. Napolitano, 20
  A. Narayan, <sup>27</sup> D. Nikolaev, <sup>20</sup> V. Owen, <sup>5</sup> C. Palatchi, <sup>11, 15</sup> J. Pan, <sup>10</sup> B. Pandey, <sup>18</sup> S. Park, <sup>9, 12</sup> K.D. Paschke, <sup>11, *</sup>
     M. Petrusky, <sup>12</sup> M.L. Pitt, <sup>28</sup> S. Premathilake, <sup>11</sup> B. Quinn, <sup>13</sup> R. Radloff, <sup>22</sup> S. Rahman, <sup>10</sup> M.N.H. Rashad, <sup>11</sup>
         A. Rathnayake, <sup>11</sup> B.T. Reed, <sup>21</sup> P.E. Reimer, <sup>29</sup> R. Richards, <sup>12</sup> S. Riordan, <sup>29</sup> Y.R. Roblin, <sup>6</sup> S. Seeds, <sup>14</sup>
       A. Shahinyan,<sup>30</sup> P. Souder,<sup>23</sup> M. Thiel,<sup>31</sup> Y. Tian,<sup>23</sup> G.M. Urciuoli,<sup>32</sup> E.W. Wertz,<sup>5</sup> B. Wojtsekhowski,<sup>6</sup> B. Yale,<sup>5</sup> T. Ye,<sup>12</sup> A. Yoon,<sup>33</sup> W. Xiong,<sup>23,34</sup> A. Zec,<sup>11</sup> W. Zhang,<sup>12</sup> J. Zhang,<sup>12,15,34</sup> and X. Zheng<sup>11</sup>
                                           <sup>1</sup>Idaho State University, Pocatello, Idaho 83209, USA
                                 <sup>2</sup> Texas A & M University - Kingsville, Kingsville, Texas 78363, USA
                                 <sup>3</sup>University of Zagreb, Faculty of Science, Zagreb, HR 10002, Croatia
                           <sup>4</sup> California State University, Los Angeles, Los Angeles, California 90032, USA
                                           <sup>5</sup> William & Mary, Williamsburg, Virginia 23185, USA
                       <sup>6</sup> Thomas Jefferson National Accelerator Facility, Newport News, Virginia 23606, USA
                           <sup>7</sup> Istituto Nazionale di Fisica Nucleare, Sezione di Catania, 95123 Catania, Italy
                                       <sup>8</sup>Louisiana Tech University, Ruston, Louisiana 71272, USA
                                    <sup>9</sup> Mississippi State University, Mississippi State, MS 39762, USA
                                     <sup>10</sup>University of Manitoba, Winnipeg, Manitoba R3T2N2 Canada
                                      <sup>11</sup> University of Virginia, Charlottesville, Virginia 22904, USA
                         <sup>12</sup>Stony Brook, State University of New York, Stony Brook, New York 11794, USA
                                   <sup>13</sup>Carnegie Mellon University, Pittsburgh, Pennsylvania 15213, USA
                                       <sup>14</sup> University of Connecticut, Storrs, Connecticut 06269, USA
                           <sup>15</sup>Center for Frontiers in Nuclear Science, Stony Brook, New York 11794, USA
                                    <sup>16</sup>Brookhaven National Laboratory, Upton, New York 11973, USA
                        <sup>17</sup>Institute for Advanced Computational Science, Stony Brook, New York 11794, USA
                                           <sup>18</sup> Hampton University, Hampton, Virginia 23668, USA
                             <sup>19</sup> University of Massachusetts Amherst, Amherst, Massachusetts 01003, USA
                                       <sup>20</sup> Temple University, Philadelphia, Pennsylvania 19122, USA
                                         <sup>21</sup> Indiana University, Bloomington, Indiana 47405, USA
                                                <sup>22</sup>Ohio University, Athens, Ohio 45701, USA
                                         <sup>23</sup>Syracuse University, Syracuse, New York 13244, USA
                                     <sup>24</sup> University of Winnipeg, Winnipeg, Manitoba R3B2E9 Canada
                                            <sup>25</sup> Jožef Stefan Institute, SI-1000 Ljubljana, Slovenia
                    <sup>26</sup>Faculty of Mathematics and Physics, University of Ljubljana, SI-1000 Ljubljana, Slovenia
                                        <sup>27</sup> Veer Kunwar Singh University, Ara, Bihar 802301, India
                                              <sup>28</sup> Virginia Tech, Blacksburg, Virginia 24061, USA
                            <sup>29</sup>Physics Division, Argonne National Laboratory, Lemont, Illinois 60439, USA
              <sup>30</sup>A. I. Alikhanyan National Science Laboratory (Yerevan Physics Institute), Yerevan 0036, Armenia
                         <sup>31</sup>Institut für Kernphysik, Johannes Gutenberg-Universität, Mainz 55122, Germany
                                              <sup>32</sup>INFN - Sezione di Roma, I-00185, Rome, Italy
                                <sup>33</sup>Christopher Newport University, Newport News, Virginia 23606, USA
                                         <sup>34</sup>Shandong University, Qingdao, Shandong 266237, China
                                                               (Dated: June 20, 2022)
```

We report a precise measurement of the parity-violating asymmetry $A_{\rm PV}$ in the elastic scattering of longitudinally polarized electrons from $^{48}{\rm Ca}$. We measure $A_{\rm PV}=2668\pm106~({\rm stat})\pm40~({\rm syst})$ parts per billion, leading to an extraction of the neutral weak form factor $F_{\rm W}(q=0.8733~{\rm fm}^{-1})=0.1304\pm0.0052~({\rm stat})\pm0.0020~({\rm syst})$ and the charge minus the weak form factor $F_{\rm ch}-F_{\rm W}=0.0277\pm0.0055$. The resulting neutron skin thickness $R_n-R_p=0.121\pm0.026~({\rm exp})\pm0.024~({\rm model})$ fm is relatively thin yet consistent with many model calculations. The combined CREX and PREX results will

have implications for future energy density functional calculations and on the density dependence of the symmetry energy of nuclear matter.

Parity-violating electron scattering (PVES) can locate neutrons in nuclei with minimal model dependence since the electroweak reaction is free from most strong interaction uncertainties [1–3]. PVES measurements can be optimized to extract the thickness of the neutron skin, the excess in the root mean-square size of the distribution of neutrons over that of the protons, which depends on the pressure of neutron-rich matter as neutrons are pushed out against surface tension [4]. Recently PREX-2 accurately measured the thickness of the neutron skin in ²⁰⁸Pb using this technique [5].

Chiral effective field theory can predict neutron skin thicknesses using two- and three-nucleon interactions [6]. These interactions are typically measured in few-nucleon systems where important three-neutron forces [7] are difficult to probe. Although such calculations using coupled cluster wave functions for both ⁴⁸Ca and ²⁰⁸Pb have now been performed [6, 8], microscopic calculations are more feasible in the lighter ⁴⁸Ca system than for ²⁰⁸Pb. We report here on a PVES measurement to constrain the neutron radius of ⁴⁸Ca. While the ²⁰⁸Pb nucleus more closely approximates uniform nuclear matter, the ⁴⁸Ca nucleus lies in a different regime of smaller nuclei for which the neutron skin is more closely related to the details of the nuclear force. Not only is the new measurement complementary to the earlier ²⁰⁸Pb result in this way, but it will allow direct comparison to more microscopic calculations.

More accurate neutron skin predictions across the periodic table [9-11] will be facilitated by these measurements in ⁴⁸Ca and ²⁰⁸Pb. Since atomic parity violation experiments depend on the overlap of atomic electrons with neutrons, PVES neutron radii constraints along with nuclear theory may allow more precise low energy tests of the Standard Model [12–15]. Coherent neutrinonucleus elastic scattering depends on neutron radii and the same weak form factor as does PVES [16, 17]. PVES weak form factor measurements along with theory may improve sensitivity to non-standard neutrino interactions. A neutron star is 18 orders of magnitude larger than a heavy nucleus yet they have similar density, and both systems are governed by the same strong interactions and equation of state relating pressure to density. [3, 18–21]. Therefore, laboratory neutron skin measurements have important implications for neutron star properties, such as radius and tidal deformability [22], and are complementary to direct X-ray [23] and gravitational wave observations [24–30].

Information on the 48 Ca weak charge distribution is obtained by measuring the PVES asymmetry ($A_{\rm PV}$) of longitudinally polarized electrons off an isotopically enriched 48 Ca target in Hall A at Thomas Jefferson National Accelerator Facility (JLab). At first Born approx-

imation, A_{PV} for a spin-zero nucleus is proportional to the ratio of weak (F_{W}) to charge (F_{ch}) form factors as [2]:

$$A_{\rm PV} = \frac{\sigma_R - \sigma_L}{\sigma_R + \sigma_L} \approx \frac{G_{\rm F} Q^2}{4\pi\alpha\sqrt{2}} \frac{|Q_W| F_{\rm W}(q)}{Z F_{\rm ch}(q)}, \qquad (1)$$

where $\sigma_{\rm R}$ ($\sigma_{\rm L}$) is the elastic differential cross-section of right (left) handed electrons off the target with a four-momentum transfer squared Q², $q = \sqrt{Q^2}$. G_F is the Fermi constant, α is the fine structure constant, and the weak charge of ⁴⁸Ca is $Q_{\rm W} = -26.0 \pm 0.1$ [31]. $F_{\rm ch}$ from existing measurements [31, 32] is used to extract $F_{\rm W}$ from the measured $A_{\rm PV}$. The requirements for the practical application of this formula including precise Coulomb distortion calculations [33] are described elsewhere [2].

With the PREX-2 apparatus [5] reoptimized to measure scattering from the calcium target, A_{PV} was measured at a four-momentum transfer just below the first diffractive cross-section minimum of ⁴⁸Ca to achieve high sensitivity to the neutron skin. Using two dipole magnets, 4° - 6° scattered electrons from a 2.18 GeV beam impinging on the calcium target were directed through precisely-machined collimators into the acceptance of the two High-Resolution Spectrometers (HRSs) [34] placed symmetrically on either side of the beam-axis. The elastically scattered electrons were focused into a peak with a momentum dispersion of about 16 m, and intercepted by a single Cherenkov detector in each HRS arm consisting of a $16 \,\mathrm{cm} \times 3.5 \,\mathrm{cm} \times 0.5 \,\mathrm{cm}$ fused-silica tile. Total internal reflection provided efficient Cherenkov light transmission to a photo-multiplier tube (PMT) coupled to the tile. The edge of the tile was positioned to ensure a momentum cut-off at ~ 2 MeV below the elastic peak. thus minimizing contributions from inelastic scattering.

The polarized electron beam was generated using circularly polarized laser light incident on a photocathode [35]. The beam polarization sign follows the handedness of the laser circular polarization selected at 120 Hz using a Pockels cell, creating 8.13 ms time windows of constant beam helicity arranged in quartet patterns (+--+ or -++-) to ensure cancellation of 60 Hz AC power pickup. The sign of each quartet was selected pseudo-randomly and reported to the data acquisition system (DAQ) with a delay to suppress electronic pickup.

Production data totaling 412 Coulombs were acquired with a 150 μ A beam rastered over a 4 mm² area on enriched ⁴⁸Ca targets mounted on a cryogenically cooled copper ladder. Two 1 g/cm² targets, with atomic ⁴⁸Ca percent of 95.99 \pm 0.02% and 91.70 \pm 0.01% were used to acquire 7.8% and 92.2% of the total data, respectively.

The PMT anode current from the \approx 28 MHz scattered flux in each detector was integrated and digitized over each helicity window by high-precision 18-bit sam-

pling ADCs. The PMT was bench-tested before and after the run using light sources mimicking the integrated Cherenkov light response to determine linearity under operating conditions. Linearity was cross-checked throughout the run by monitoring detector output variation with beam current. The independent asymmetry measurements from each HRS were combined with equal weight; the final data set comprised 87M window quartets.

The beam intensity, energy and trajectory at the target were measured with beam monitors using the same integrating DAQ. Three radio frequency (RF) cavities (BCMs) measured the beam intensity, while six RF antenna monitors (BPMs) measured beam position along the beam line, including at dispersive locations with energy sensitivity. The polarized source was tuned to minimize the average helicity-correlated changes in beam parameters on target [36]. Two techniques were used to reverse the beam polarization relative to the voltage applied to the Pockels cell. A half-wave plate (HWP) was inserted in the laser beam path, separating the data sets into alternating reversal states with a period of about ten hours. The full production data set was additionally divided into three parts characterized by a change in spin precession in the low energy injector which reversed (or not) the polarization sign on target relative to that at the polarized source. Averaging over these reversals further suppressed spurious helicity-correlated asymmetries in A_{PV} .

The helicity-correlated integrated beam charge asymmetry was controlled using active feedback, and averaged to -89 ppb over the run. Modulations of air-core magnets and an accelerating RF cavity placed upstream of all BPMs were used to calibrate detector sensitivities. This calibration was crosschecked with a regression analysis based on intrinsic beam fluctuations. The individual quartet measurements of $A_{\rm PV}$ were corrected for beam intensity, trajectory and energy fluctuations; the helicity-correlated correction averaged to 53 ± 5 ppb over the run. Consistency checks demonstrated that the residual detector asymmetry fluctuations were dominated by counting statistics.

Two polarimeters measured the longitudinal beam polarization P_b upstream of the target. Operating continuously through the run, the Compton polarimeter used a calorimeter to measure the energy of photons scattered by the electron beam traversing an optical cavity of circularly polarized green laser light [37]. Calibration uncertainties were minimized by integrating the calorimeter response for each helicity window, thereby eliminating a low-energy threshold. Another polarimeter that detected Møller-scattered electrons from a polarized iron foil target in a 4 T magnetic field was deployed 9 times periodically during the run. The results were consistent between polarimeters and combined to yield $P_b = 87.10 \pm 0.39\%$.

Calibration data were collected at reduced beam current (100 nA to 1 μ A) to enable counting and tracking

of individual electrons. With Cherenkov detector PMT gains increased to detect individual particle pulses in coincidence with drift chamber tracks and trigger scintillators hits, the reconstructed scattering angle and momentum were calibrated using scattered electrons from a thin carbon target and a steel-walled water flow target, mounted on a separate, water-cooled target ladder. The momentum recoil difference between elastic scattering from hydrogen and oxygen in the water target calibrates the central angle to 0.02° absolute accuracy.

Similar counting data collected with the production 48 Ca target were used to estimate the fractional contribution from the first three low-lying excited states in 48 Ca, which totaled 1.4% of the accepted rate. Calculation of the excited state asymmetries and conservative uncertainties [31] lead to the $A_{\rm PV}$ corrections listed in Table I. The 48 Ca parity-conserving transverse single-spin asymmetry $A_{\rm T}$ was independently measured [38] and, along with counting data, used to estimate a 13 ppb uncertainty in the $A_{\rm T}$ correction to $A_{\rm PV}$, due to potential residual transverse beam polarization coupled to imperfect symmetry in the left-right and top-bottom acceptance.

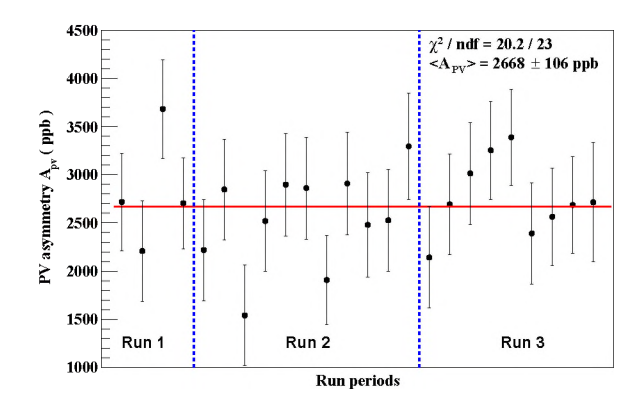


FIG. 1. Measurements of $A_{\rm PV}$ with statistical uncertainty; each $\approx \! 40$ hour period includes two states with complementary HWP settings. The three run periods demarcate injector spin orientation reversals.

Using a theoretically computed $A_{\rm PV}(^{40}{\rm Ca}) = 2430 \pm 30~{\rm ppb}$ [31], the $A_{\rm PV}$ contribution from the assayed 7.95% $^{40}{\rm Ca}$ target fraction was calculated to be 19 \pm 3 ppb. Figure 1 shows $A_{\rm PV}$ measurements after all corrections in roughly uniform periods, with the global average $A_{\rm PV} = 2668 \pm 106~{\rm ppb}$.

To compare this result to a theoretical model, the acceptance function $\epsilon(\theta)$ provides the distribution of scattering angles intercepting the Cherenkov detectors:

$$\langle \mathbf{A} \rangle = \frac{\int d\theta \, \sin\theta \, \mathbf{A}(\theta) \, \frac{d\sigma}{d\Omega} \, \epsilon(\theta)}{\int d\theta \, \sin\theta \, \frac{d\sigma}{d\Omega} \, \epsilon(\theta)} \tag{2}$$

where $\frac{d\sigma}{d\Omega}$ is the differential cross-section and A(θ) is the modeled parity violating asymmetry as a function of scattering angle [39]. Simulation modeling of the calibration

data was used to calculate $\epsilon(\theta)$. Radiative and rescattering effects in the target change the average accepted angle by 1.5%. The mean kinematics were found to be $\langle\theta\rangle=4.51^{\circ}\pm0.02^{\circ}$ and $\langle Q^{2}\rangle=0.0297~\pm~0.0002~({\rm GeV/c})^{2}$. Alternative acceptance functions, calculated using geometric and magnetic tolerances but still constrained to match spectra from calibration runs, were used to calculate an uncertainty of ±24 ppb on $A_{\rm PV}$ due to possible variation of $\epsilon(\theta)$.

TABLE I. $A_{\rm PV}$ corrections and corresponding systematic uncertainties, normalized to account for polarization and background fractions.

Correction	Absolute [ppb]	Relative [%]
Beam polarization	382 ± 13	14.3 ± 0.5
Beam trajectory & energy	68 ± 7	2.5 ± 0.3
Beam charge asymmetry	112 ± 1	4.2 ± 0.0
Isotopic purity	19 ± 3	0.7 ± 0.1
$3.831 \text{ MeV } (2^+) \text{ inelastic}$	-35 ± 19	-1.3 ± 0.7
$4.507 \text{ MeV } (3^{-}) \text{ inelastic}$	0 ± 10	0 ± 0.4
$5.370 \text{ MeV } (3^-) \text{ inelastic}$	-2 ± 4	-0.1 ± 0.1
Transverse asymmetry	0 ± 13	0 ± 0.5
Detector non-linearity	0 ± 7	0 ± 0.3
Acceptance	0 ± 24	0 ± 0.9
Radiative corrections (Q_W)	0 ± 10	0 ± 0.4
Total systematic uncertainty	40 ppb	1.5%
Statistical uncertainty	106 ppb	4.0%

Table I lists all significant corrections and corresponding uncertainties; the total systematic uncertainty is 40 ppb.

The weak form factor is directly related to $A_{\rm PV}$ in Eqn 1, and is the Fourier transform of the weak charge density $\rho_{\rm W}$,

$$F_{\rm W}(q) = \frac{1}{Q_{\rm W}} \int d^3r \, j_0(qr) \rho_{\rm W}(r).$$
 (3)

We assume a shape for $\rho_W(r)$ and calculate $A_{\rm PV}$, including Coulomb distortions and integrating over the acceptance $\epsilon(\theta)$. After adjusting the radius parameter in the $\rho_W(r)$ model [31] to reproduce the measured $A_{\rm PV}$, we evaluate $F_W(q)$ in Eq. 3 using this $\rho_W(r)$ at the reference momentum transfer $q=0.8733~{\rm fm}^{-1}$. This procedure is insensitive to the form of the model ρ_W and yields the results in Table II.

While the extracted value of $F_{\rm W}$ depends on $F_{\rm ch}$, $F_{\rm W}/F_{\rm ch}$ and $F_{\rm ch}-F_{\rm W}$ are quite insensitive to $F_{\rm ch}$. In order to determine $F_{\rm ch}(q)=\int d^3r\,j_0(qr)\rho_{\rm ch}(r)/Z$, we use a composite charge density for ⁴⁸Ca starting with an accurate sum of Gaussians density for ⁴⁰Ca [40] and add a Fourier Bessel expansion for the small difference between the charge densities of ⁴⁸Ca and ⁴⁰Ca [32, 41], see [31]. This procedure yields a ⁴⁸Ca charge radius of 3.481 fm, close to the experimental value of 3.477 fm [42].

TABLE II. CREX form factor results for 48 Ca, with q and $F_{\rm ch}$ input values. The uncertainties are due to statistics and experimental systematics, respectively.

Quantity	Value	±	(stat)	±	(sys)
q	0.8733				0.0104
$F_{ m W}(q)/F_{ m ch}(q) \ F_{ m ch}(q)$	0.8248 0.1581	±	0.0328	±	0.0124
$F_{ m W}(q)$	0.1304				
$F_{\rm ch}(q) - F_{\rm W}(q)$	0.0277	±	0.0052	±	0.0020

A main result of this paper is a measurement of the difference between charge and weak form factors,

$$F_{\rm ch}(q) - F_{\rm W}(q) = 0.0277 \pm 0.0055 \text{ (exp)}.$$
 (4)

The uncertainty is the quadrature sum of the experimental statistical and systematic uncertainties, referred to henceforth as the experimental error (exp), dominated by counting statistics. We emphasize that the Eq. 4 result is model-independent and quite insensitive to the assumed shape for the weak density $\rho_W(r)$.

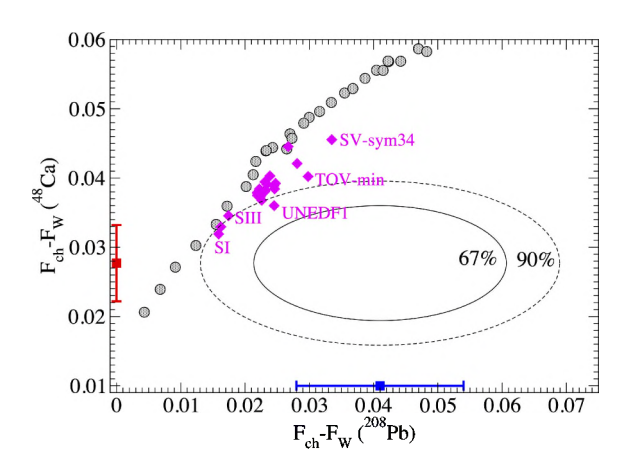


FIG. 2. Difference between the charge and weak form factors of ⁴⁸Ca (CREX) versus that of ²⁰⁸Pb (PREX-2) at their respective momentum transfers. The blue (red) data point shows the PREX-2 (CREX) measurements. The ellipses are joint PREX-2 and CREX 67% and 90% probability contours. The gray circles (magenta diamonds) are a range of relativistic (non-relativistic) density functionals. For clarity only some of these functionals are labeled. The complete list is in ref. [31].

Figure 2 displays Eq. 4 for 48 Ca along with the PREX-2 result $F_{\rm ch} - F_{\rm W} = 0.041 \pm 0.013$ for 208 Pb at a smaller momentum transfer of 0.3977 fm $^{-1}$ [5]. The figure also shows a series of relativistic energy functional models with density-dependent symmetry energy slope parameter L [43, 44] that varies over a large range from small negative values at the lower left to large positive values at the upper right. Additionally, a diverse collection of non-relativistic density functional models are

shown [31]. Here, $F_{\rm ch}$ and $F_{\rm W}$ include proton and neutron densities folded with single nucleon electric and magnetic form factors and spin orbit currents [45]. The models that best reproduce both the CREX and PREX-2 results tend to predict $F_{\rm ch} - F_{\rm W}$ slightly below the PREX-2 result for ²⁰⁸Pb and slightly above the CREX result for ⁴⁸Ca.

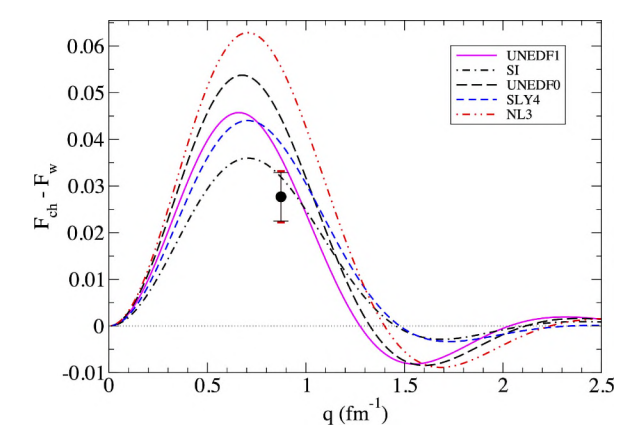


FIG. 3. The difference between the charge and weak form factors for 48 Ca as a function of momentum transfer $q = \sqrt{Q^2}$. The curves show results for non-relativistic (SI, SLY4, UN-EDF0, UNEDF1) and relativistic (NL3) density functional models. The CREX measurement is indicated by a circle with the inner black error bar showing the contribution from statistics and the total experimental error bar in red.

Figure 3 shows the momentum transfer dependence of $F_{\rm ch}-F_{\rm W}$ as predicted by a few non-relativistic and relativistic density functional models. It is evident that some model results cross as a function of q, emphasizing the somewhat different q dependence. In the limit $q \to 0$, $F_{\rm ch}(q)-F_{\rm W}(q)\approx q^2(R_{\rm W}^2-R_{\rm ch}^2)/6$, where $R_{\rm W}$ is the rms radius of $\rho_W(r)$ and $R_{\rm ch}$ is the charge radius. Since this equation is not valid at the larger q of CREX, the extraction of $R_{\rm W}-R_{\rm ch}$ introduces some model dependence.

Relativistic and non-relativistic density functional model predictions of $R_{\rm W}-R_{\rm ch}$ are plotted in Fig. 4(a) versus $F_{\rm ch}(q)-F_{\rm W}(q)$. The somewhat different $\rho_W(r)$ shapes lead to the vertical spread in the non-relativistic models. Figure 4(b) shows a similar plot of point neutron minus proton radii R_n-R_p versus $F_{\rm ch}(q)-F_{\rm W}(q)$. To calculate R_n-R_p given $F_{\rm ch}-F_{\rm W}$ one must include full current operators including spin orbit $(\vec{L}\cdot\vec{S})$ contributions [41]. Relativistic models tend to have somewhat larger $\vec{L}\cdot\vec{S}$ currents. As a result the gray circles in Fig. 4(b) are somewhat lower than those in Fig. 4(a) when compared to non-relativistic models. Lines with slope matching that of the relativistic model variation are drawn to enclose the full range of displayed models, providing the model range and central values listed in

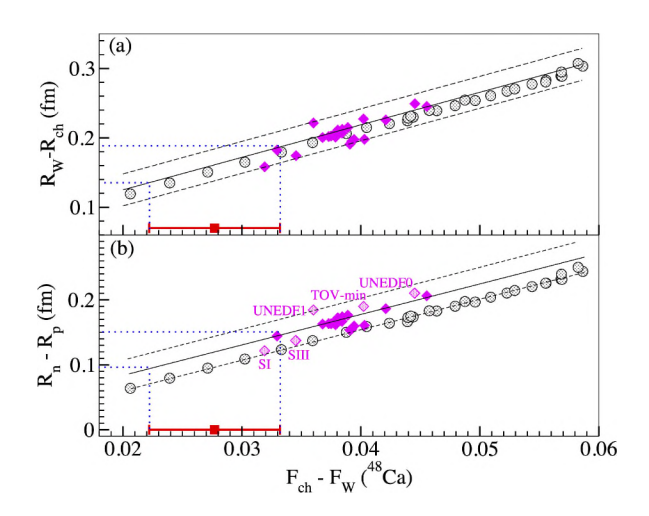


FIG. 4. (a) ⁴⁸Ca weak minus charge rms radius versus charge minus weak form factor at the CREX momentum transfer. The CREX experimental value and uncertainty is shown (red square). The gray circles (magenta diamonds) show a range of relativistic (non-relativistic) density functionals. (b) ⁴⁸Ca neutron minus proton rms radius versus charge minus weak form factor.

Table III. This underscores the fact that the CREX ⁴⁸Ca $R_n - R_p$ has significant modeling uncertainty, in contrast to the PREX ²⁰⁸Pb $R_n - R_p$, see [31]. Reduced model uncertainty would result if theoretical predictions were compared to the model-independent $F_{\rm ch} - F_{\rm W}$ in Fig. 2 rather than to $R_n - R_p$ in Fig. 5.

TABLE III. Extracted $R_{\rm W} - R_{\rm ch}$ and $R_n - R_p$ radii. The first uncertainty is experimental and the second reflects the shape uncertainty in $\rho_W(r)$ estimated from the spread in Fig. 4.

	•
Quantity	Value \pm (exp) \pm (model) [fm]
$R_{\rm W} - R_{\rm ch} R_n - R_p$	$0.159 \pm 0.026 \pm 0.023$ $0.121 \pm 0.026 \pm 0.024$

 $R_n - R_p$ for ⁴⁸Ca versus $R_n - R_p$ for ²⁰⁸Pb is shown in Fig. 5. A number of models including the microscopic coupled cluster calculations [8] are consistent with our results, slightly under-predicting ²⁰⁸Pb while slightly over-predicting ⁴⁸Ca. Dispersive optical model calculations agree well for ²⁰⁸Pb but substantially over-predict $R_n - R_p$ for ⁴⁸Ca [46].

In conclusion, we have reported a new and precise measurement of the PVES asymmetry from $^{48}\mathrm{Ca}$ and a model-independent extraction of the difference between the charge form factor and the weak form factor $F_\mathrm{ch}-F_\mathrm{W}$ at $q=0.8733~\mathrm{fm}^{-1}$. In addition, we have extracted, with a small model dependence, the weak skin $R_\mathrm{W}-R_\mathrm{ch}$ and the neutron skin R_n-R_p of $^{48}\mathrm{Ca}$ and compared it to that of $^{208}\mathrm{Pb}$. The extracted neutron skin of $^{48}\mathrm{Ca}$ (CREX) is relatively thin compared to the prediction of most mod-

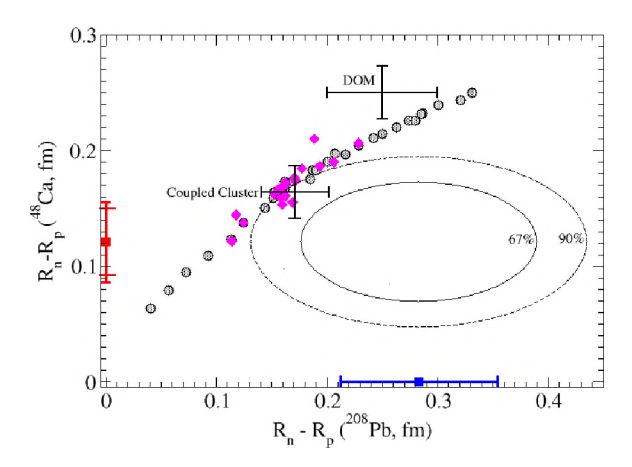


FIG. 5. ⁴⁸Ca neutron minus proton radius versus that for ²⁰⁸Pb. The PREX-2+PREX-1 experimental result is shown as a blue square, while that for CREX is shown as a red square with the inner error bars indicating the experimental error and the outer error bars including the model error. The gray circles (magenta diamonds) show a variety of relativistic (non-relativistic) density functionals. Coupled cluster [8] and dispersive optical model (DOM) predictions [46] are also shown.

els, while that of ²⁰⁸Pb (PREX) is thick, yet both are consistent with a number of density functional models and with the microscopic coupled cluster models [8]. This will have implications for future energy density functional calculations and the density dependence of the symmetry energy.

The small model dependence of this result could be further constrained with a future measurement of $A_{\rm PV}$ from $^{48}{\rm Ca}$ at an additional Q^2 [47]. Experimental techniques from this work, including excellent systematic control of helicity-correlated fluctuations and demonstration of high precision electron beam polarimetry, will inform the design of future projects MOLLER [48] and SoLID [49] at JLab measuring fundamental electroweak couplings, as well as P2 and the $^{208}{\rm Pb}$ radius experimental proposals at Mainz [50].

We thank the entire staff of JLab for their efforts to develop and maintain the polarized beam and the experimental apparatus, and acknowledge the support of the U.S. Department of Energy, the National Science Foundation and NSERC (Canada). We thank J. Piekarewicz, P. G. Reinhard and X. Roca-Maza for RPA calculations of 48 Ca excited states and J. Erler and M. Gorchtein for calculations of $\gamma-Z$ radiative corrections. This material is based upon the work supported by the U.S. Department of Energy, Office of Science, Office of Nuclear Physics Contract No. DE- AC05-06OR23177.

- paschke@virginia.edu
- T. Donnelly, J. Dubach, and I. Sick, Isospin dependences in parity-violating electron scattering, Nuclear Physics A 503, 589 (1989).
- [2] C. J. Horowitz, S. J. Pollock, P. A. Souder, and R. Michaels, Parity violating measurements of neutron densities, Phys. Rev. C 63, 025501 (2001).
- [3] M. Thiel, C. Sfienti, J. Piekarewicz, C. J. Horowitz, and M. Vanderhaeghen, Neutron skins of atomic nuclei: per aspera ad astra, Journal of Physics G: Nuclear and Particle Physics 46, 093003 (2019).
- [4] B. Brown, Neutron radii in nuclei and the neutron equation of state, Phys. Rev. Lett. 85, 5296 (2000).
- [5] D. Adhikari et al. (PREX Collaboration), Accurate determination of the neutron skin thickness of ²⁰⁸Pb through parity-violation in electron scattering, Phys. Rev. Lett. 126, 172502 (2021).
- [6] G. Hagen et al., Neutron and weak-charge distributions of the ⁴⁸Ca nucleus, Nature Physics 12, 186 (2016).
- [7] W. Bentz and I. C. Cloët, Slope parameter of the symmetry energy and the structure of three-particle interactions in nuclear matter (2022), arXiv:2004.11605 [nucl-th].
- [8] B. Hu et al., Ab initio predictions link the neutron skin of ²⁰⁸Pb to nuclear forces (2021), arXiv:2112.01125 [nuclth].
- [9] S. J. Novario, D. Lonardoni, S. Gandolfi, and G. Hagen, Trends of neutron skins and radii of mirror nuclei from first principles (2021), arXiv:2111.12775.
- [10] M. Kortelainen, J. Erler, W. Nazarewicz, N. Birge, Y. Gao, and E. Olsen, Neutron-skin uncertainties of skyrme energy density functionals, Phys. Rev. C 88, 031305(R) (2013).
- [11] F. Sammarruca, Neutron skin systematics from microscopic equations of state (2022), arXiv:2203.09753.
- [12] C. S. Wood et al., Science 275, 1759 (1970).
- [13] M. A. Bouchiat and C. Bouchiat, Rept. Prog. Phys. 60, 1351 (1997).
- [14] M. J. Ramsey-Musolf, Low-energy parity-violation and new physics, Phys. Rev. C 60, 015501 (1999).
- [15] M. S. Safronova, D. Budker, D. DeMille, D. F. J. Kimball, A. Derevianko, and C. W. Clark, Search for new physics with atoms and molecules, Rev. Mod. Phys. 90, 025008 (2018).
- [16] D. Akimov et al., Observation of coherent elastic neutrino-nucleus scattering, Science 357, 1123 (2017).
- [17] D. Akimov et al., First measurement of coherent elastic neutrino-nucleus scattering on argon, Phys. Rev. Lett. 126, 012002 (2021).
- [18] S. J. Novario, G. Hagen, G. R. Jansen, and T. Papen-brock, Charge radii of exotic neon and magnesium isotopes, Phys. Rev. C 102, 051303(R) (2020).
- [19] H. Shen, F. Ji, J. Hu, and K. Sumiyoshi, Effects of symmetry energy on the equation of state for simulations of core-collapse supernovae and neutron-star mergers, The Astrophysical Journal 891, 148 (2020).
- [20] C. Horowitz, Neutron rich matter in the laboratory and in the heavens after GW170817, Annals of Physics 411, 167992 (2019).
- [21] J. B. Wei, J. J. Lu, G. F. Burgio, Z. H. Li, and H. J. Schulze, Are nuclear matter properties correlated to neutron star observables?, Eur. Phys. J. A 56, 63 (2020).

- [22] F. J. Fattoyev, J. Piekarewicz, and C. J. Horowitz, Neutron skins and neutron stars in the multimessenger era, Phys. Rev. Lett. 120, 172702 (2018).
- [23] T. E. Riley et al., A NICER view of PSR j0030+0451: Millisecond pulsar parameter estimation, The Astrophysical Journal 887, L21 (2019).
- [24] K. Chatziioannou, Neutron-star tidal deformability and equation-of-state constraints, Gen. Rel. Grav. 52, 109 (2020).
- [25] Y. Zhang, M. Liu, C.-J. Xia, Z. Li, and S. K. Biswal, Constraints on the symmetry energy and its associated parameters from nuclei to neutron stars, Phys. Rev. C 101, 034303 (2020).
- [26] H. Güven, K. Bozkurt, E. Khan, and J. Margueron, Multimessenger and multiphysics bayesian inference for the GW170817 binary neutron star merger, Phys. Rev. C 102, 015805 (2020).
- [27] L. Baiotti, Gravitational waves from neutron star mergers and their relation to the nuclear equation of state, Progress in Particle and Nuclear Physics 109, 103714 (2019).
- [28] J. Piekarewicz and F. J. Fattoyev, Constraints on the symmetry energy and its associated parameters from nuclei to neutron stars, Physics Today 72, 30 (2019).
- [29] M. Tsang, W. Lynch, P. Danielewicz, and C. Tsang, Symmetry energy constraints from GW170817 and laboratory experiments, Physics Letters B 795, 533 (2019).
- [30] M. Fasano, T. Abdelsalhin, A. Maselli, and V. Ferrari, Constraining the neutron star equation of state using multiband independent measurements of radii and tidal deformabilities, Phys. Rev. Lett. 123, 141101 (2019).
- [31] See Supplemental Material [url], which includes Ref. [51–77], for more information. (2022).
- [32] H. J. Emrich, G. Fricke, G. Mallot, H. Miska, H. G. Sieberling, J. M. Cavedon, B. Frois, and D. Goutte, Radial distribution of nucleons in isotopes ^{48,40}Ca., Nucl. Phys. A 396, 401C (1983).
- [33] C. J. Horowitz, Parity violating elastic electron scattering and coulomb distortions, Phys. Rev. C 57, 3430 (1998).
- [34] J. Alcorn et al., Basic instrumentation for Hall A at Jefferson Lab, Nuclear Instruments and Methods in Physics Research Section A: Accelerators, Spectrometers, Detectors and Associated Equipment 522, 294 (2004).
- [35] C. K. Sinclair et al., Development of a high average current polarized electron source with long cathode operational lifetime, Phys. Rev. ST Accel. Beams 10, 023501 (2007).
- [36] C. Palatchi and K. Paschke, RTP Pockels cell with nanometer-level position control (2021), arXiv:2106.09546.
- [37] M. Friend et al., Upgraded photon calorimeter with integrating readout for Hall A Compton Polarimeter at Jefferson Lab, Nucl. Instrum. Meth. A 676, 96 (2012), arXiv:1108.3116 [physics.ins-det].
- [38] D. Adhikari et al. (PREX, CREX), New Measurements of the Beam-Normal Single Spin Asymmetry in Elastic Electron Scattering over a Range of Spin-0 Nuclei, Phys. Rev. Lett. 128, 142501 (2022).
- [39] See Supplemental Material [url] for a table of this function. (2022).
- [40] I. Sick, J. Bellicard, J. Cavedon, B. Frois, M. Huet, P. Leconte, P. Ho, and S. Platchkov, Charge density of 40Ca, Physics Letters B 88, 245 (1979).
- [41] H. de Vries, C. W. de Jager, and C. de Vries, Nuclear

- Charge-Density-Distribution Parameters from Electron Scattering, Atomic Data and Nuclear Data Tables **36**, 495 (1987).
- [42] G. Fricke and K. Heilig, Nuclear charge radii · 20-Ca calcium: Datasheet from Landolt-Börnstein Group i elementary particles, nuclei and atoms · volume 20: "nuclear charge radii" in SpringerMaterials (2004), copyright 2004 Springer-Verlag Berlin Heidelberg.
- [43] J. W. Holt and Y. Lim, Universal correlations in the nuclear symmetry energy, slope parameter, and curvature, Physics Letters B 784, 77 (2018).
- [44] X. Viñas, M. Centelles, X. Roca-Maza, and M. Warda, Density dependence of the symmetry energy from neutron skin thickness in finite nuclei, The European Physical Journal A 50, 27 (2014).
- [45] C. J. Horowitz and J. Piekarewicz, Impact of spin-orbit currents on the electroweak skin of neutron-rich nuclei, Phys. Rev. C 86, 045503 (2012).
- [46] M. C. Atkinson, M. H. Mahzoon, M. A. Keim, B. A. Bordelon, C. D. Pruitt, R. J. Charity, and W. H. Dickhoff, Dispersive optical model analysis of ²⁰⁸Pb generating a neutron-skin prediction beyond the mean field, Phys. Rev. C 101, 044303 (2020).
- [47] B. T. Reed, Z. Jaffe, C. J. Horowitz, and C. Sfienti, Measuring the surface thickness of the weak charge density of nuclei, Phys. Rev. C 102, 064308 (2020).
- [48] J. Benesch et al. (MOLLER Collaboration), The MOLLER experiment: An ultra-precise measurement of the weak mixing angle using Møller scattering, arXiv:1411.4088 (2014).
- [49] P. Souder et al., (SoLID Collaboration), Precision measurement of parity-violation in deep inelastic scattering over a broad kinematic range, Technical Report No. JLAB-PR-09-012-pvdis, TJNAF (2008).
- [50] D. Becker *et al.*, The P2 experiment, Eur. Phys. J. A 54, 208 (2018).
- [51] B. G. Todd-Rutel and J. Piekarewicz, Neutron-Rich Nuclei and Neutron Stars: A New Accurately Calibrated Interaction for the Study of Neutron-Rich Matter, Phys. Rev. Lett. 95, 122501 (2005), arXiv:nucl-th/0504034 [astro-ph].
- [52] B. Dreher, J. Friedrich, K. Merle, H. Rothhaas, and G. Lührs, The determination of the nuclear ground state and transition charge density from measured electron scattering data, Nuclear Physics A 235, 219 (1974).
- [53] I. Angeli and K. P. Marinova, Table of experimental nuclear ground state charge radii: an update, Atomic Data and Nuclear Data Tables 99, 69 (2013).
- [54] P.A. Zyla et al. (Particle Data Group), 2020 review of particle physics, Prog. Theor. Exp. Phys. 2020, 083C01 (2020).
- [55] M. Gorchtein and C. J. Horowitz, Dispersion γ Z-box correction to the weak charge of the proton, Phys. Rev. Lett. **102**, 091806 (2009).
- [56] Jens Erler and Misha Gorchtein, Private communication (2022).
- [57] G. A. Lalazissis, J. Konig, and P. Ring, A new parametrization for the Lagrangian density of relativistic mean field theory, Phys. Rev. C 55, 540 (1997), arXiv:nucl-th/9607039.
- [58] T. H. R. Skyrme, The effective nuclear potential, Nuclear Physics 9, 615 (1958).
- 59] J. E. Wise, J. S. McCarthy, R. Altemus, B. E. Norum, R. R. Whitney, J. Heisenberg, J. Dawson, and O. Schwen-

- tker, Inelastic electron scattering from 48 Ca, Phys. Rev. C **31**, 1699 (1985).
- [60] R. A. Eisenstein, D. W. Madsen, H. Theissen, L. S. Cardman, and C. K. Bockelman, Electron-Scattering Studies on ⁴⁰Ca and ⁴⁸Ca, Phys. Rev. 188, 1815 (1969).
- [61] A. M. Bernstein, V. R. Brown, and V. A. Madsen, Neutron and proton transition matrix elements and inelastic hadron scattering, Physics Letters B 103, 255 (1981).
- [62] J. R. Vanhoy, M. T. McEllistrem, S. F. Hicks, R. A. Gatenby, E. M. Baum, E. L. Johnson, G. Molnár, and S. W. Yates, Neutron and proton dynamics of 48 Ca levels and γ -ray decays from neutron inelastic scattering, Phys. Rev. C **45**, 1628 (1992).
- [63] P. G. Reinhard and X. Roca-Maza, Private communication (2022).
- [64] J. Piekarewicz, Private communication (2022).
- [65] W.-C. Chen and J. Piekarewicz, Searching for isovector signatures in the neutron-rich oxygen and calcium isotopes, Physics Letters B 748, 284 (2015), arXiv:1412.7870 [nucl-th].
- [66] B. T. Reed, F. J. Fattoyev, C. J. Horowitz, and J. Piekarewicz, Implications of PREX-2 on the equation of state of neutron-rich matter, Phys. Rev. Lett. 126, 172503 (2021), arXiv:2101.03193 [nucl-th].
- [67] W.-C. Chen and J. Piekarewicz, Building relativistic mean field models for finite nuclei and neutron stars, Phys. Rev. C 90, 044305 (2014), arXiv:1408.4159 [nuclth].
- [68] F. Fattoyev, C. Horowitz, J. Piekarewicz, and G. Shen, Relativistic effective interaction for nuclei, giant resonances, and neutron stars, Phys. Rev. C 82, 055803 (2010), arXiv:1008.3030 [nucl-th].
- [69] F. J. Fattoyev and J. Piekarewicz, Has a thick neutron

- skin in 208 Pb been ruled out?, Phys. Rev. Lett. **111**, 162501 (2013), arXiv:1306.6034 [nucl-th].
- [70] D. Vautherin and D. M. Brink, Hartree-Fock Calculations with Skyrme's Interaction. I. Spherical Nuclei, Phys. Rev. C 5, 626 (1972).
- [71] J. Bartel, P. Quentin, M. Brack, C. Guet, and H. B. Håkansson, Towards a better parametrisation of Skyrmelike effective forces: A critical study of the SkM force, Nuc. Phys. A 386, 79 (1982).
- [72] E. Chabanat, P. Bonche, P. Haensel, J. Meyer, and R. Schaeffer, A Skyrme parametrization from subnuclear to neutron star densities Part II. Nuclei far from stabilities, Nuc. Phys. A 635, 231 (1998).
- [73] P. Klüpfel, P. G. Reinhard, T. J. Bürvenich, and J. A. Maruhn, Variations on a theme by Skyrme: A systematic study of adjustments of model parameters, Phys. Rev. C 79, 034310 (2009).
- [74] J. Erler, C. J. Horowitz, W. Nazarewicz, M. Rafalski, and P. G. Reinhard, Energy density functional for nuclei and neutron stars, Phys. Rev. C 87, 044320 (2013), arXiv:1211.6292 [nucl-th].
- [75] M. Kortelainen, T. Lesinski, J. Moré, W. Nazarewicz, J. Sarich, N. Schunck, M. V. Stoitsov, and S. Wild, Nuclear energy density optimization, Phys. Rev. C 82, 024313 (2010).
- [76] M. Kortelainen, J. McDonnell, W. Nazarewicz, P.-G. Reinhard, J. Sarich, N. Schunck, M. V. Stoitsov, and S. M. Wild, Nuclear energy density optimization: Large deformations, Phys. Rev. C 85, 024304 (2012).
- [77] C. J. Horowitz and J. Piekarewicz, The neutron radii of Pb-208 and neutron stars, Phys. Rev. C 64, 062802 (2001), arXiv:nucl-th/0108036.